HNUE JOURNAL OF SCIENCE
Natural Sciences 2025, Volume 70, Issue 4, pp. 57-67
This paper is available online at http://hnuejs.edu.vn/ns
DOI: 10.18173/2354-1059.2025-0054

MICROSATELLITE HYBRID STRUCTURE USING ALUMINUM 7075-T6 AND CFRP FOR IMPROVED LAUNCH PERFORMANCE SURVIVABILITY

Nguyen Thuy Linh[2], Nguyen Cong Thai[3], Le Xuan Huy[1] and To Anh Duc[1*]
[1]*Vietnam National Space Center, Vietnam Academy of Science and Technology, Hanoi city, Vietnam*
[2]*University of Science and Technology of Hanoi, Vietnam Academy of Science and Technology, Hanoi city, Vietnam*
[3]*Staff Agency of the Air Defence - Air Force Service, Hanoi city, Vietnam*
*Corresponding author: To Anh Duc, e-mail: taduc@vnsc.org.vn

Received August 5, 2025. Revised December 14, 2025. Accepted December 30, 2025.

Abstract. This study presents the structural design and simulation of a 50 kg-class microsatellite developed for compatibility with the JAXA Epsilon launch vehicle. A hybrid architecture combining Aluminum 7075-T6 and Carbon Fiber Reinforced Polymer (CFRP) was employed to meet stringent mass, stiffness, and vibration requirements. The final structure, measuring 480 × 488 × 550 mm, achieved a total mass of 45 kg, falling within the required launch envelope. Finite element simulations were conducted using ANSYS 2024R2 to evaluate modal, sine-sweep, random vibration, and shock responses under launch-induced conditions. The first three natural frequencies, 118.99 Hz (X-axis), 123.77 Hz (Y-axis), and 240.42 Hz (Z-axis), surpassed the required thresholds, avoiding resonance with vehicle-induced excitations. Vibration analyses confirmed that peak acceleration responses remained within safe operational margins, with sine-sweep, random vibration, and shock responses showing no modal amplification. Component-level stress simulations revealed von Mises stress values well below material limits across all critical subsystems. These results validate the structural integrity and dynamic survivability of the hybrid microsatellite, demonstrating its readiness for spaceflight.

Keywords: microsatellite, hybrid structure, aluminum 7075-T6, CFRP, vibration analysis, finite element simulation.

1. Introduction

Background & Motivation: Over the past two decades, the small satellite sector has undergone a profound transformation driven by the demand for cost-effective access to space, rapid deployment cycles, and the miniaturization of satellite subsystems [1]-[4]. To address strict JAXA Epsilon rideshare constraints, material selection therefore

becomes a central aspect of spacecraft structural design, requiring a careful balance between mass-efficiency, mechanical robustness, and dynamic stability under harsh launch environments [5]-[8].

Novelty & Objectives: This research utilizes a hybrid structure optimized for the 40–65 kg mass range. Aluminum 7075-T6 provides high tensile strengths (~572 x 10^6 Pa) and yield (~5.05 x 10^8 Pa) strengths and robust interfaces for elements such as the Lightband® separation system, whereas CFRP laminates can reach tensile strengths up to 1,500 x 10^6 Pa at a density of about 1.72 g/cm³, making them suitable for side panels, thermal enclosures, and other non-primary load paths [9]-[12]. The design aims to fit a 600×600×800 mm envelope and achieve natural frequencies significantly above the 80 Hz (Z) and 40 Hz (X/Y) thresholds.

2. Content

2.1. Methodology

A microsatellite structure (480×488×550 mm) was developed using CATIA V5 to maximize volume utilization within the JAXA Epsilon envelope (600×600×800 mm). The design features a modular panel frame supporting multifunctional integration and subsystems (ADCS, CDHS, payload, power). ANSYS finite element analysis evaluated load-bearing members, specifically isogrid panels and T-shaped connectors, under launch conditions defined by the JAXA Epsilon User Manual. Modal analysis confirmed that natural frequencies avoid launcher excitation, while boundary conditions and mesh refinements adhered to ECSS standards to ensure accurate load transfer through the 8-inch Lightband® interface.

2.2. CAD modelling

The primary structure ($480 \times 488 \times 550$ mm) ensures optimal component arrangement and compliance with the Epsilon launch envelope, as shown in Figure 1a. Aluminum 7075-T6 is utilized for all major load-bearing components due to its high specific strength, while CFRP side plates are employed to reduce mass without compromising stiffness. This hybrid configuration yields a total mass of ~45 kg, remaining well within the required limits.

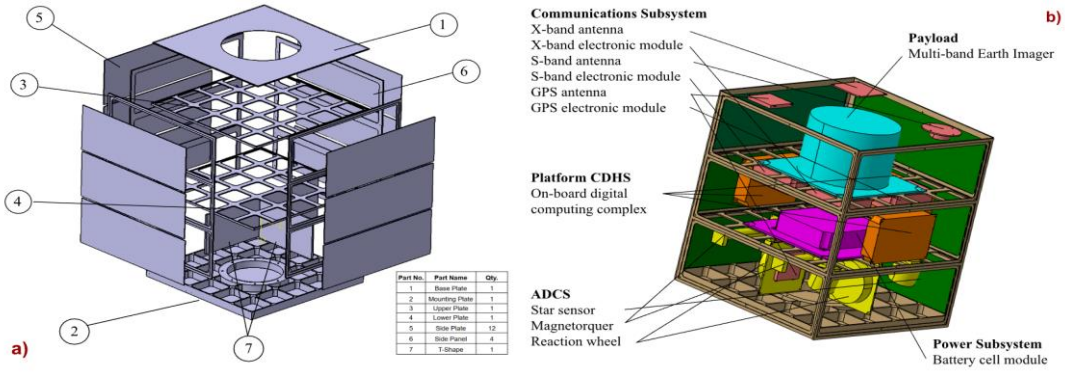

Figure 1. (a) View of the microsatellite primary structure designed using CATIA V5; (b) Structural configuration of small satellite subsystems

Table 1 and Figure 1b detail the configuration of the six main subsystems. The Multi-Band Earth Imager (MBEI) payload is positioned at the front to ensure an unobstructed nadir view and shock isolation, while ADCS components are arranged symmetrically to minimize torque and isolate sensitive sensors. Communication antennas are placed on the upper plate for optimal coverage, the CDHS is mounted near the base to optimize cabling and radiation shielding, and the battery unit is located near the center of mass to maintain dynamic balance and reduce thermal gradients.

Table 1. List of the main subsystems and volume of components of the small satellite

Subsystem	**Component**	**Quantity**	**Single-Unit Volume (cm^3)**
Payload	Multi-band earth imager	1	4000
ADCS	Star sensor	2	31.76
	Magnetorquer	3	23.99
	Reaction wheel	4	57.42
Communications subsystem	X-band antenna	1	19.09
	S-band antenna	3	0.21
	GPS antenna	2	25.50
	Antenna module	4	530.8
Platform CDHS	On-board digital computing complex	3	213.1
Power subsystem	Battery cell module	1	216.2
Structural subsystem	Satellite structure	set	9000
	Component mounting bracket	-	584
Satellite total volume			16400

Standard metric bolts ensure structural integrity: M2 × 6 mm fasteners secure lightweight electronics, M3 × 10 mm bolts anchor heavier subsystems (payload, battery), and M4 × 8 - 10 mm bolts connect the main aluminum frame to reinforce rigidity. All fasteners are fully modeled in CAD and simulation to verify clearance, mass distribution, and realistic launch behavior.

2.3. Mass and center of gravity

The Center of Gravity (C.G.) of the satellite was calculated using CATIA V5 through the "Measure Inertia" function, applied to the complete 3D assembly model (Table 2). This function helps verify whether the C.G. is within acceptable ranges for launch vehicle integration and dynamic stability. The C.G. was determined relative to the geometric coordinate system, with the origin defined at the structural center

$$C.G. = (X, Y, Z) = (-2.414, -0.085, 7.799)\ mm \quad (1)$$

Table 2. Moment of inertia matrix of the small satellite

Axis	x-column	y-column	z-column	Unit
x	0.735	8.1×10^{-4}	0.01	kg.m^2
y	8.1×10^{-4}	0.0661	-0.001	kg.m^2
z	0.01	-0.001	0.509	kg.m^2

This slight offset is expected, resulting from the asymmetric placement of internal components, and remains well within the permissible bounds for launch integration and attitude control. Furthermore, Table 3 confirms that the satellite's center of gravity falls entirely within the allowable limits of the launch system along all three axes. This is critical to maintaining dynamic balance and ensuring compatibility during integration with the launch vehicle.

Table 3. Comparison of computed C.G. with launcher requirements

Axis	Computed C.G. (mm)	Allowed Range (mm)	Result
X	-2.414	±5	Within limit
Y	-0.085	±5	Within limit
Z	7.799	±15	Within limit

The inertia matrix is another key dynamic property that reflects how mass is distributed within the satellite and how it resists rotation around each axis. The values were obtained using the “Measure Inertia” tool in CATIA V5, based on the complete satellite 3D model. The resulting matrix (Table 2) is expressed as follows:

$$\mathrm{SRS}(\omega_n) = t_{\max} \left| x(t; \omega_n, \xi) \right| \tag{2}$$

The diagonal elements I_{xx}, I_{yy}, I_{zz} represent the satellite’s resistance to rotation around the X, Y, and Z axes, respectively. These values are balanced and close in magnitude, indicating a symmetric mass distribution. The off-diagonal elements, I_{xy}, I_{xz}, I_{yz}, are very small, close to zero. This suggests that the satellite has minimal asymmetry or unbalanced mass, which is favorable for rotational stability. A near-diagonal inertia matrix like this is desirable in satellite design, as it simplifies attitude control and helps prevent unexpected tumbling during flight.

2.4. Finite element simulation

The finite element model was generated in ANSYS using 3D quadratic elements. The main structural components were meshed predominantly with 10-node tetrahedral solid elements SOLID187, while a limited number of 20-node brick elements SOLID186 were introduced in locally regular regions. Slender connectors and fixtures were idealized as BEAM188 Timoshenko beam elements. Boundary conditions were applied by fully constraining the nodes on the interface surface with the launcher adapter and leaving the remaining external faces traction-free, ensuring that rigid-body motions were removed without over-constraining the structure.

2.4.1. Mesh refinement

To ensure numerical reliability, the mesh was refined iteratively from a coarse baseline under constant boundary conditions. At each step, static and modal parameters (stress, displacement, frequency) were compared, with local densification applied at high-gradient regions like material interfaces. The mesh in Figure 2 was selected once further refinement yielded negligible changes in results relative to computational cost.

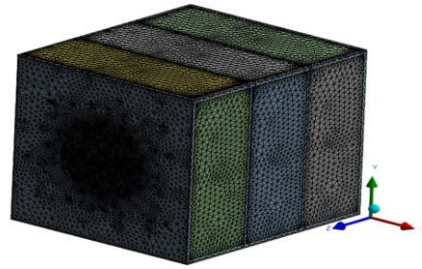

Figure 2. The mesh of the structure in the FEM model

2.4.2. Modal analysis

The natural frequencies of the satellite were evaluated along all three axes to verify compliance with the launcher's vibration requirements. As summarized in Table 4, the first modes in all directions exceed the specified limits, confirming that the structure satisfies the modal criteria for launch.

Table 4. Natural frequency requirements for three axes

Axis	Requirement (Hz)	Frequency (Hz)
X_{SC}	≥ 40	118.99
Y_{SC}	≥ 40	123.77
Z_{SC}	≥ 80	240.42

The microsatellite's first three natural frequencies (119, 123, and 240 Hz) are relatively high for the 50 kg class, primarily due to the high stiffness of Aluminum 7075-T6 isogrid decks and a short ~170 mm effective bending span. Although the lateral structure consists of bolted side panels rather than a monolithic frame, the connections create closed load paths that enhance global bending and torsional stiffness. With the ~45 kg FEM mass consistent with the system budget, these elevated frequencies represent a genuinely stiff structural configuration rather than artifacts of unrealistically low mass or over-constrained boundaries.

2.4.3. Sinusoidal vibration analysis

To assess the microsatellite's structural response, a sine sweep analysis was conducted per the JAXA Epsilon multi-payload launch ICD, utilizing fully constrained base plate interfaces and vibratory input at the Lightband® interface. In the 43 - 53 Hz range, acceleration amplitude grew linearly from approximately 9.0 m/s² to just above 9.0 m/s² without mode excitation, while the 53 - 57 Hz band exhibited less than 2% variation and no resonance, despite its proximity to the first natural frequency. Consequently, the response remained fully stable and free of dynamic amplification across both ranges, confirming the structural configuration satisfies acceptable launch acceleration thresholds.

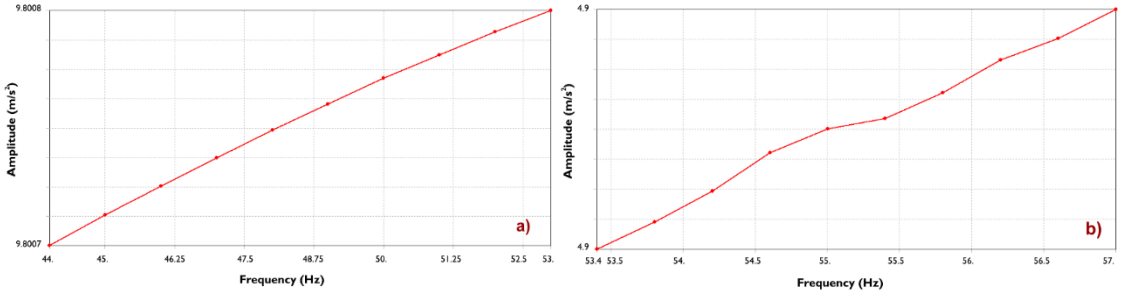

Figure 3. Measured acceleration amplitude during the sine sweep excitation from a) 43 Hz to 53 Hz, and b) 53 Hz to 57 Hz

2.4.4. Random vibration analysis

The random vibration response was evaluated using JAXA Epsilon User's Manual (Rev A, July 2018) PSD inputs, with results for all three axes shown in Figure 4. To simulate stochastic launch conditions, a simultaneous 1-sigma PSD (G^2/Hz) profile - featuring a rising slope, mid-frequency plateau, and high-frequency roll-off - was applied to all axes with fully constrained baseplate interfaces.

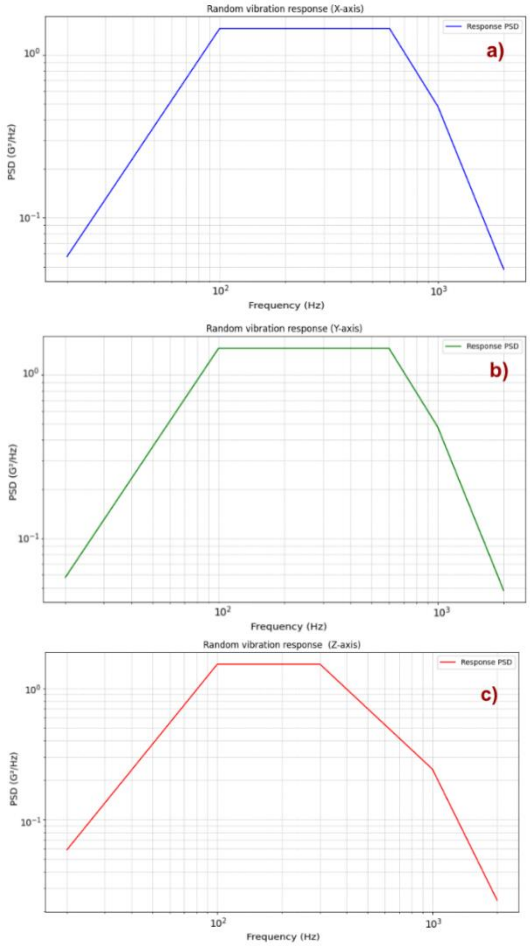

Figure 4. Directional acceleration response of the satellite structure under random vibration: a) X-axis, b) Y-axis, and c) Z-axis

Figures 4a and 4b show identical X and Y axis behavior, reflecting structural symmetry: a rise to a stable 100–600 Hz plateau followed by a high-frequency decrease, with no unexpected resonances. The Z-axis (Figure 4c) follows this pattern but exhibits a steeper roll-off beyond 1 kHz, consistent with the vertical stiffness of the stacked deck configuration. Across all axes, response profiles track the input PSD shape without abnormal peaks, confirming the absence of problematic amplification and validating the design for the 40 - 65 kg class.

2.4.5. Shock analysis

The shock response was performed according to the standard shock environment defined in the JAXA multi-launch specification for microsatellites with a mass range of 40 - 65 kg.

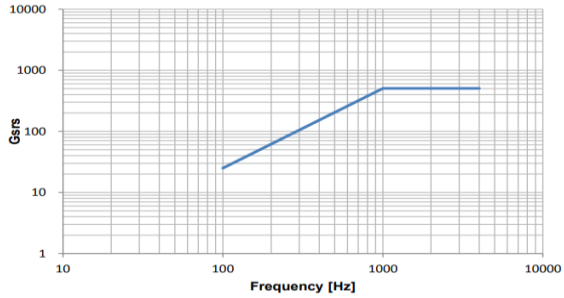

Figure 5. Input shock response spectrum for 40-60kg PL

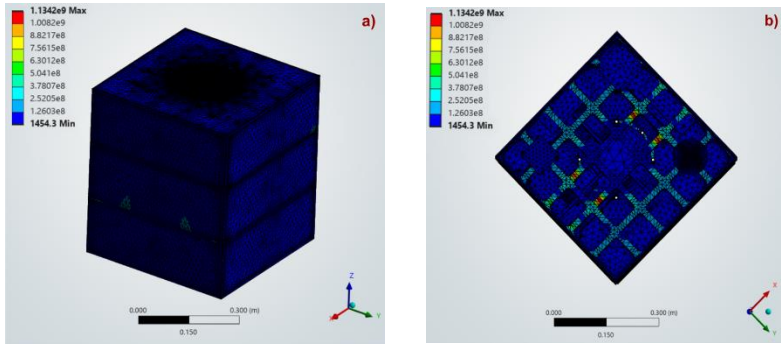

Figure 6. a) Contour of effective stress of the model (unit: Pa), b) Contour of effective stress on the top perforated face of the model (unit: Pa)

A damping ratio of Q = 10 (approximately 5% critical damping) was applied per the JAXA standard SRS environment to filter high-frequency noise while preserving flexural mode amplification. Shock loading was implemented via a response-spectrum method, defining the SRS as the oscillator response $x(t)$ under the base acceleration history.

$$\mathrm{MOS}_{\mathrm{yield}} = \frac{\sigma_{\mathrm{yield}}}{\sigma_{\mathrm{FEA}}\,\mathrm{FS}_{\mathrm{yield}}} - 1 \tag{3}$$

Modal superposition covered modes up to the 4 kHz cutoff, showing mostly low response (Figure 6a). However, localized stress peaks reaching ~1.134×10^{9} Pa were observed at geometric discontinuities near the upper interface (Figure 6b), driven by the heavy MBEI and limited isogrid stiffness. These peaks are spatially confined and do not compromise global integrity. The absence of spurious artifacts validates the methodology,

while results suggest strengthening the isogrid or panel stiffness around the MBEI footprint to eliminate these concentrations in future revisions.

2.5. Structural analysis

2.5.1. Composite material modelling and failure criteria

The composite panel comprises four 0.2 mm CFRP plies (0.8 mm total) arranged in a balanced 0°/90°/0°/90° stacking sequence to match aerospace-grade prepreg standards. The 0° plies provide axial stiffness while 90° plies stabilize the transverse direction, creating a near quasi-isotropic behavior that distributes stress evenly. Failure is assessed using the Tsai-Hill criterion, expressed as

$$F_{\mathrm{TH}} = \left(\frac{\sigma_1}{X_t}\right)^2 - \frac{\sigma_1\sigma_2}{X_t Y_t} + \left(\frac{\sigma_2}{Y_t}\right)^2 + \left(\frac{\tau_{12}}{S}\right)^2 \tag{4}$$

with failure at $F_{TH} = 1$. In ANSYS, the reported inverse reserve factor corresponds directly to F_{TH}. The simulation yields a maximum IRF of 0.303, showing that the laminate remains far from any critical condition. The safety factor is defined relative to the Tsai-Hill critical stress

$$\mathrm{FOS} = \frac{\sigma_{\mathrm{crit}}}{\sigma_{\mathrm{eff}}} \tag{5}$$

The corresponding safety margin is

$$\mathrm{MOS}_{\mathrm{TH}} = \frac{\sigma_{\mathrm{crit}} - \sigma_{\mathrm{eff}}}{\sigma_{\mathrm{eff}}} \tag{6}$$

In this work, the Tsai-Hill criterion is used exclusively to evaluate the CFRP panels, and all composite safety factors are derived from this failure index. For Tsai-Hill, the inverse reserve factor can be interpreted as 0.3. The minimum values obtained, FOS=3.297 and MOS=2.297, are therefore well above typical minimum qualification criteria for composite spacecraft structures (on the order of FOS ≥ 1.4 in launch applications), indicating a very comfortable safety margin before reaching the Tsai-Hill failure surface. While this laminate is well-suited for the static mechanical analysis presented here, its suitability may change if future work incorporates thermal or thermo-mechanical loading, where differing thermal expansion directions may require adjustments to the ply count or stacking sequence. Within the scope of the present study, however, the 0°/90°/0°/90° layup with 0.2 mm plies provides an efficient, manufacturable, and robust configuration with ample safety margin.

2.5.2. Static analysis

To define static analysis loads, Table 1 components were modeled as individual masses on the main structure. Per GSFC-STD-7000A, inertial loads were evaluated along the three principal axes using launcher limit accelerations (a_X, a_Y, a_Z) to capture peak ascent conditions. For a component of mass m_i, the inertial force in direction j is

$$F_{i,j} = m_i a_j \tag{7}$$

The corresponding moment acting on the spacecraft structure arises from the offset

between the component's center of mass and the satellite reference frame. This moment is obtained using

$$M_{i,j} = \mathbf{r}_i \times \mathbf{F}_{i,j} \tag{8}$$

where r_i is the center of mass vector. In FEM, global acceleration was applied to the assembly to assess local attachment loads. Component stresses were evaluated against material limits per GSFC-STD-7000A safety factors. Margins of safety were computed using

$$\mathrm{MOS}_{\mathrm{yield}} = \frac{\sigma_{\mathrm{yield}}}{\sigma_{\mathrm{FEA}}\,\mathrm{FS}_{\mathrm{yield}}} - 1 \tag{9}$$

Equations (7)-(9) are applied only to metallic components such as the aluminum frames, brackets, and antenna supports. Positive margins across all loading directions indicate that the structure satisfies the quasi-static strength requirements without requiring additional reinforcement or design modifications.

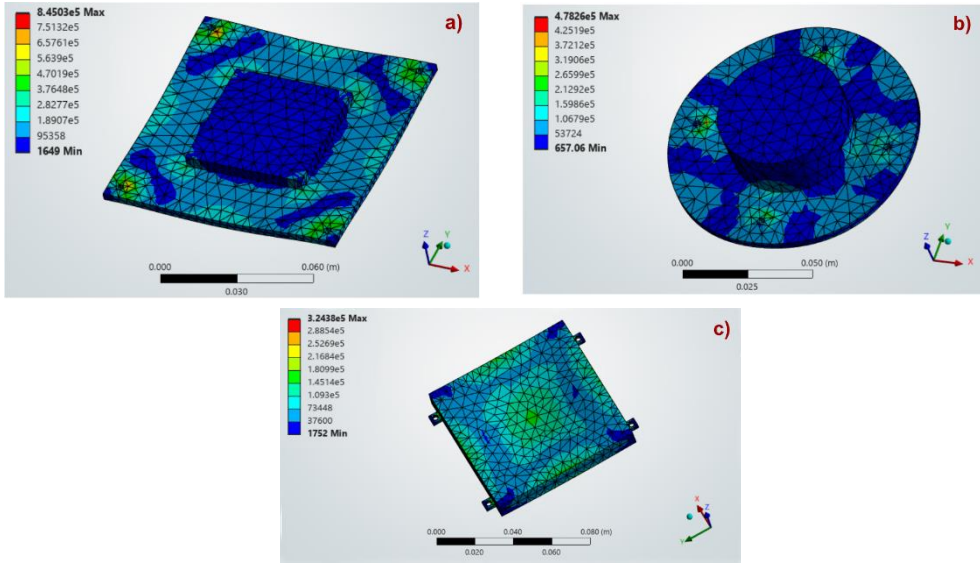

Figure 7. von Mises Stress Distribution in the metallic support structures of the: a) S-band antenna; b) X-band antenna; and c) GPS antenna (unit: Pa)

- *S-band antenna:* the peak stress is 8.4503 x 10^5 Pa, giving a very high FOS of 595.3. The load spreads evenly across the surface, with no notable stress concentrations (Figure 7a).

- *X-band antenna:* the maximum stress reached 4.782 x 10^5 Pa, corresponding to a FOS of around 1,052.3. Its simple, lightweight geometry keeps stress levels low under launch conditions (Figure 7b).

- *GPS antenna*: a maximum von Mises stress of about 3.2438 x 10^5 Pa, resulting in a FOS of 1,552.5. The stress distribution is smooth, with only minor variations near the mounts and no critical hotspots (Figure 7c).

- *Magnetorquer:* a very low peak von Mises stress of 2.412 x 10^4 Pa, leading to an extremely high FOS of 2170.5. This shows the part is far stronger than needed and remains safe under launch loading (Figure 8a).

- *Star sensor:* a maximum stress of 1.125 x 10^6 Pa, yielding a FoS of 450.8. Although this is lower than the other components, it still meets all safety margins and does not show

any critical stress areas (Figure 8b).

- *Reaction wheel:* peaking at 5.2211 x 10^5 Pa, which results in a healthy FOS of 963.4. The stresses remain moderate and well distributed, confirming that the design is strong without adding unnecessary mass (Figure 8c).

- *Battery module:* the battery enclosure shows the highest stress at 1.3743 x 10^6 Pa, but still achieves a high FOS of 366.0. The stress pattern is smooth overall, with only small increases at the corners and no risky concentrations (Figure 8d).

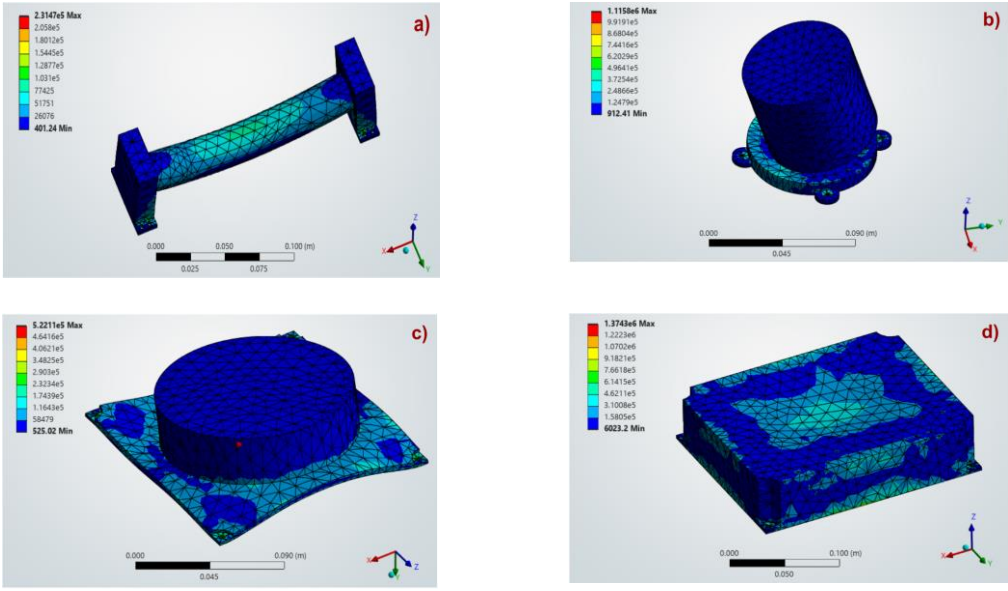

Figure 8. von Mises Stress Distribution in the metallic support structures of the a) Magnetorquer; b) Star sensor; c) Reaction wheel; d) Battery module enclosure

3. Conclusions

This study demonstrated the viability of a hybrid structural design employing Aluminum 7075-T6 for primary load-bearing members and CFRP for mass-optimized external panels. The Aluminum-CFRP structure meets the required natural frequency margins along all three axes, avoiding resonant coupling with launcher excitations. Under the prescribed sine and random vibration loads, it exhibits a stable broadband response in the 120-630 Hz range without significant modal amplification or structural degradation.

Component-level stress analysis validated mechanical reliability, showing that quasi-static and random vibration stresses remained well below the Aluminum 7075-T6 yield strength (5.05×10^8 Pa) with safety factors ranging from 366 to over 2,170. Although shock analysis identified localized peaks reaching 1.134×10^9 Pa at geometric discontinuities, these were confined to the isogrid surface and did not compromise global integrity. Consequently, while the primary frame is robust, increasing isogrid rib thickness and fillet radii at payload interfaces is recommended to better distribute transient shock loads and reduce stress concentrations.

Overall, stress magnitudes followed predictable mass and support patterns with no critical hotspots affecting fatigue life or load-path integrity. While von Mises applicability

is limited for non-metallics, consistently low values confirm global structural integrity within the mixed-material architecture. This hybrid design effectively balances stiffness and mass efficiency to meet launch and orbital requirements, providing a robust foundation for future multifunctional integrations such as thermal control, sensors, or radiation shielding.

Acknowledgments. This study was financially supported by the Ministry of Science and Technology under grant KC.13.03/21-30.

REFERENCES

[1] Saito T, Kuwahara T, Saito Y & Sato Y, (2025). Guidance strategies for controlled Earth reentry of small spacecraft in low Earth orbit. *Acta Astronautica*, 229, 684-697.

[2] Gomez I, Aplin KL, Lawrie A & Toomer CA, (2024). Modelling an Ion Thruster for a Small Spacecraft in Very Low Earth Orbit. *Journal of Physics: Conference Series (IOP Publishing)*, 2702(1), 012019.

[3] Sedelinkov A, Nikolaeva A, Serdakova V & Khnyryova E, (2024). Technologies for Increasing the Control Efficiency of Small Spacecraft with Solar Panels by Taking into Account Temperature Shock. *Technologies*, 12(10), 207.

[4] Mahendrakar T, White RT, Tiwari M & Wilde M, (2024). Unknown non-cooperative spacecraft characterization with lightweight convolutional neural networks. *Journal of Aerospace Information Systems*, 21(5), 455-460.

[5] Ince JC, Peerzada M, Mathews LD, Pai AR, Al-Qatatsheh A, Abbasi S & Salim NV, (2023). Overview of emerging hybrid and composite materials for space applications. *Advanced Composites and Hybrid Materials*, 6(4), 130.

[6] Oropeza D, Seager T, Firdosy S, Guerra J, Billings K, Jones JP & Roberts S, (2024). Porosity control of copper-based alloys via powder bed fusion additive manufacturing for spacecraft applications. *Journal of Porous Materials*, 31(2), 779-791.

[7] Goto A, Umeda K, Yukumatsu K & Kimoto Y, (2021). Property changes in materials due to atomic oxygen in the low Earth orbit. *CEAS Space Journal*, 13(3), 415-432.

[8] Pernigoni L & Grande AM, (2023). Advantages and challenges of novel materials for future space applications. *Frontiers in Space Technologies*, 4, 1253419.

[9] Nishihara K, Okuyama KI, Rodriguez R & Fajardo I, (2024). The Thermo-Mechanical Properties of Carbon-Fiber-Reinforced Polymer Composites Exposed to a Low Earth Orbit Environment. *Aerospace*, 11(3), 201.

[10] Lopresti S, Abiti A, Olivieri L, Giacomuzzo C, Polli EM & Francesconi A, (2024). A Numerical Model for CFRP Fragmentation Under Hypervelocity Impacts. *75th International Astronautical Congress*, 1-9.

[11] Di Trani N, Masini A, Bo T, Paci MM, Batra JS, Reggiani M & Grattoni A, (2024). Probing physicochemical performances of 3D printed carbon fiber composites during 8-month exposure to space environment. *Advanced Functional Materials*, 34(13), 2310243.

[12] Watson E, Murillo JLS, Durr N & Ledford N, (2024). Simulating impact-induced satellite breakups with a discrete element method. *Acta Astronautica*, 219, 428-437.